CHAPTER 5

STRUCTURAL, DIELECTRIC, FERROELECTRIC AND IMPEDANCE SPECTROSCOPIC STUDIES ON $Ba_{1-x}Sr_xTiO_3$ $(0.15 \leq x \leq 0.35)$

5.1 Introduction

$Ba_{1-x}Sr_xTiO_3$ (BST) is a solid solution of perovskites $BaTiO_3$ and $SrTiO_3$ covering the whole range of x (0 to 1) with Sr occupying the Ba site. The ferroelectric to paraelectric transition temperature T_c of pure $BaTiO_3$ decreases almost linearly by increasing the Sr content. In addition, the sharpness of ε' vs. temperature curve of $BaTiO_3$ becomes diffused by addition of Sr. $Ba_{1-x}Sr_xTiO_3$ has been extensively studied due to its wide variety of potential applications in energy storage devices, capacitors, microwave dielectric resonators, filters, varactors, lens antennas for electromagnetic beam stearing etc [Moulson et al. (2003); Gevorgian (2009)]. In order to assure better reproducibility and propose device designs so as to achieve optimum inter-segment power transfer, knowledge of overall electrical behavior of the system is desired. This is greatly facilitated by representing the ceramic system by a suitable equivalent circuit model and determining the values of the components used in the model. For this, the technique of impedance spectroscopy has emerged as a very powerful tool and is being widely used in various fields of science and engineering [Moulson et al. (2003); Macdonald (2005)]. This not only greatly helps in understanding the electrical behaviour of the system but also yields an equivalent circuit model that may be used in simulating and developing various applications. Surprisingly, to the best of our knowledge, no results for equivalent circuit models for $Ba_{1-x}Sr_xTiO_3$ are available.

Similarly, there are only a few reports on bulk dielectric properties of this system and that too on specific compositions in the frequency range 8-12 GHz (X band of microwaves) by some research groups [Ioachim et al. (2006); Wee et al. (2011); Teranishi et al. (2009)].

The work presented in this Chapter involves synthesis of $Ba_{1-x}Sr_xTiO_3$ (x=0.15, 0.20, 0.25, 0.30 and 0.35) system by solid state reaction method and characterization by XRD and SEM observation of ferroelectric P – E hysteresis loops, dielectric studies and impedance measurements in the frequency range 1 Hz to 1 MHz. Equivalent circuit model involving combination of Constant Phase angle Elements (CPE) and resistances (R) was developed which represents the data well. Also values of dielectric permittivity measured at microwave frequencies (8 – 12 GHz) at room temperature are reported.

5.2 Experimental

Samples of $Ba_{1-x}Sr_xTiO_3$ [(BST15 (x = 0.15), BST20 (x = 0.20), BST25 (x = 0.25), BST30 (x = 0.30) and BST35 (x = 0.35)] were prepared by conventional solid state route as described in Chapter 3. High purity powders of $BaCO_3$, $SrCO_3$ and TiO_2 (Merck 99.5%) were mixed thoroughly by ball milling for 6 hours and then calcined at 950 ^{0}C for 6 hours. The calcined powders were mixed with small amount of polyvinyl alcohol (PVA) binder and pressed into disc-like (dia 12 mm, thickness 1.5 mm) and rectangular (23 mm x 10 mm x 4 mm) pellets using uniaxial hydraulic press under 60 kN load. Binder was removed by raising the temperature to 500 °C at 2 ºC/min and holding there for 2 hours. Then the temperature was raised to 1250 ºC at 5 ºC/min and held for 6 hours followed by furnace cooling to room temperature.

Phase formation was confirmed by recording room temperature powder X-ray diffraction (XRD) patterns of the calcined and sintered powders using a Rigaku high resolution X-ray diffractometer employing Cu K_α radiation with Ni-filter in the

Phase formation was confirmed by recording room temperature powder X-ray diffraction (XRD) patterns of the calcined and sintered powders using a Rigaku high resolution X-ray diffractometer employing Cu K_α radiation with Ni-filter in the diffraction angle (2θ) range 20º- 90º. Rietveld refinement was carried out using Fullprof software. Experimental (bulk) density of the samples was determined by Archimedes principle and the percentage porosity was calculated using the formula:

$$\% \text{ porosity} = \frac{\text{theoretical density} - \text{experimental density}}{\text{theoretical density}} \text{ x } 100$$

Surface morphology was studied by Scanning Electron Microscope (ZIESS). For this, the sintered pellets were thoroughly polished using emery papers of grade 1/0 (40 μm), 2/0 (30 μm), 3/0 (20 μm) and 4/0 (10 μm) (Sia, Switzerland). The fine polishing was done on blazer cloth using 0.25 μm diamond paste of grade 1/4-OS-475 (HIFIN). The pellets were then thermally etched at a temperature 100 ^{0}C lower than the sintering temperature for about 15 minutes. The etched pellets were then gold coated.

Dielectric and impedance measurements were carried out in the frequency range 1 Hz – 1 MHz by using Novocontrol Alpha-A Analyzer. For this the disc like cylindrical pellets were polished using emery papers of grade 1/0 and 2/0 and electroded on both sides using silver paste which was cured at 600 ^{0}C for 15 minutes. Similar electroded pellets were used to measure the P-E hysteresis loops using the instrument AixACCT systems TF Analyzer 2000E, Germany. The high frequency dielectric measurements were carried out at room temperature in X-Band (8.2 GHz – 12.4 GHz) using the Keysight E5071C Network Analyzer. The rectangular pellets were placed in the X-Band rectangular waveguide which was connected to the Network Analyzer through a coaxial cable using a coaxial to waveguide adapter. The measurement technique is based on the so-called transmission line method (Nicolson-Ross-Weir method) which involves placing the sample inside a portion of an enclosed transmission line (in the present system, metallic rectangular waveguide) and measuring scattering parameters S_{11} and S_{21} which are used to obtain the dielectric properties of the material [Nicolson et al. (1970); Weir (1974)]

5.3 Results and Discussion

5.3.1 Phase analysis

X-Ray diffraction (XRD) patterns of all the samples are given in Figure 5.1. The patterns match well with the JCPDS code 44-0093 (space group P4mm) without any impurity phase peaks. Figure 5.1(b) shows the 002/200 peaks around $2\theta = 45.5^0$ for all the samples. A continuous shift towards higher 2θ is observed as the Sr content increases. This can be attributed to substitution of the smaller Sr^{2+} (ionic radius r_i =1.40 Å) on Ba^{2+} (ionic radius r_i=1.60 Å) site leading to decrease in the lattice parameters [Ioachim et al. (2006); Zhou et al. (1999)]. Also the 002 peak merges with the 200 peak with increase in Sr content. This shows decrease in tetragonality as Sr content increases as shown in Figure 5.2. This is in agreement with the results available in literature [Tiwari et al. (1995)]. Rietveld refinement (shown in Figures 5.1(c-g) gives weight to these observations as the unit cell volume $V(Å)^3$ as well as the c/a ratio decrease with increase in Sr content, as given in Table 5.1. The shoulder seen on the right end of all the 200 peaks is due to $K\alpha_2$ component of X-rays. It is observed that the structure remains tetragonal upto x = 0.35.

Various reports are available in literature about the composition (value of x) up to which the structure remains tetragonal at room temperature as described in Section 1. Our result agrees with that of Rushman and Strivens [Rushman et al. (1946)].

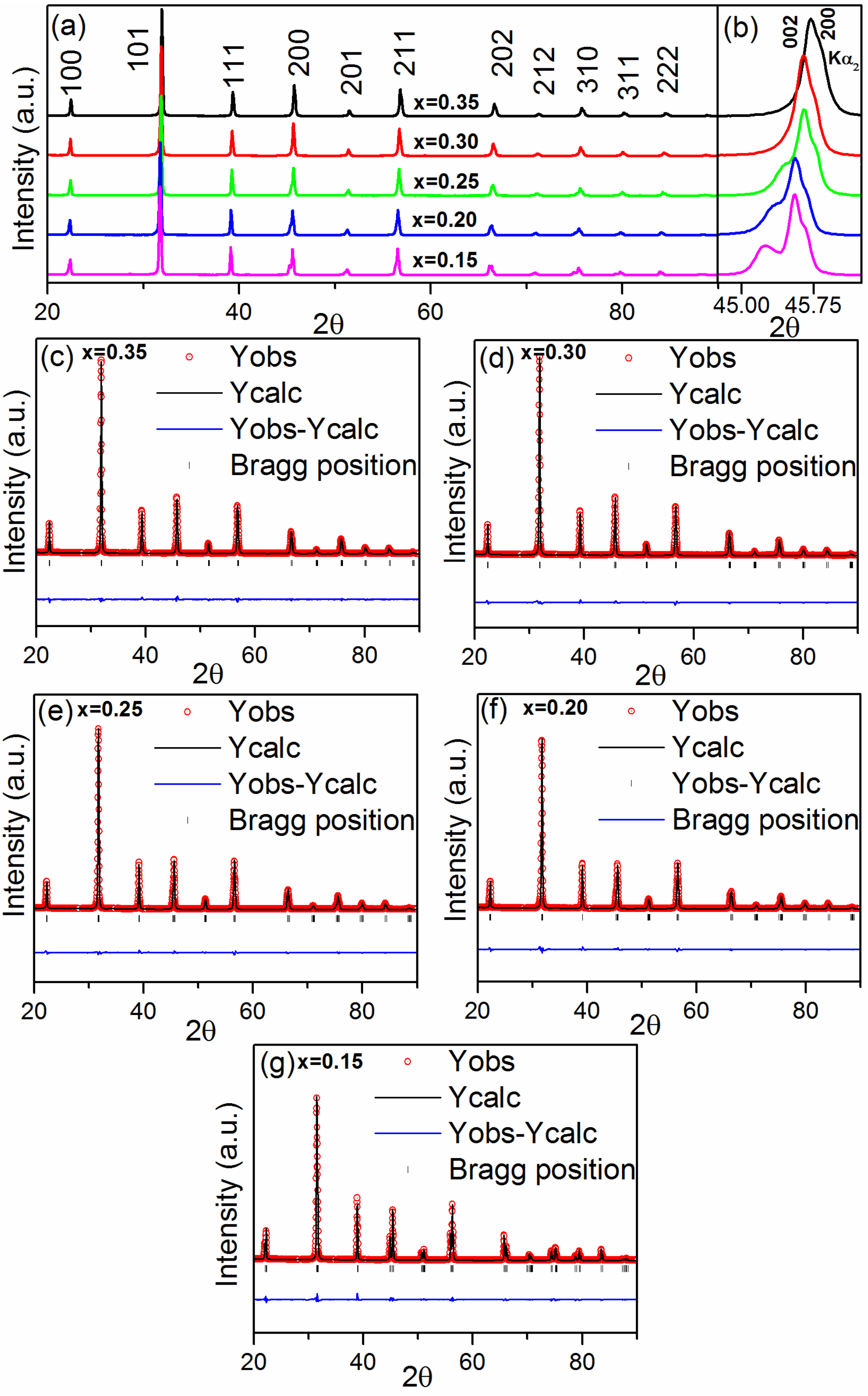

Figure 5.1: (a) XRD patterns of $Ba_{1-x}Sr_xTiO_3$ (x = 0.15, 0.20, 0.25, 0.30 and 0.35), (b) Magnified peaks around 45.5 degree, Rietveld refinement for (c) x=0.15, (d) x=0.20, (e) x=0.25, (f) x=0.30 and (g) x=0.35.

Table 5.1 : Rietveld refinement parameters for $Ba_{1-x}Sr_xTiO_3$

Composition (x)	**a(Å)**	**c(Å)**	**c/a**	**V(Å^3)**	**Bragg R-factor**	**χ^2**	**Experimental Density (gm/cc)**	**% Porosity**
0.15	3.986	4.015	1.007	63.12	1.75	3.11	5.15	13.30
0.20	3.980	4.000	1.005	63.37	1.71	2.78	5.55	5.13
0.25	3.975	3.993	1.004	63.10	1.51	2.61	5.08	12.56
0.30	3.972	3.981	1.002	62.82	1.66	2.74	5.04	13.10
0.35	3.968	3.972	1.001	62.56	1.65	2.34	5.13	9.04

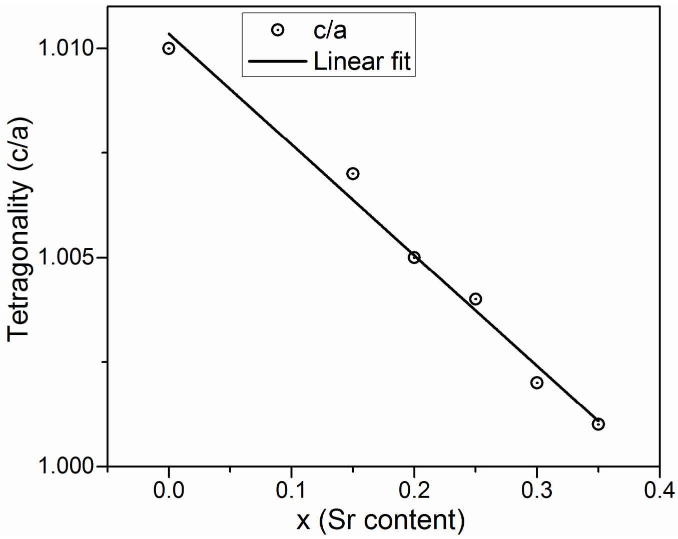

Figure 5.2: Tetragonality (c/a) versus Strontium content.

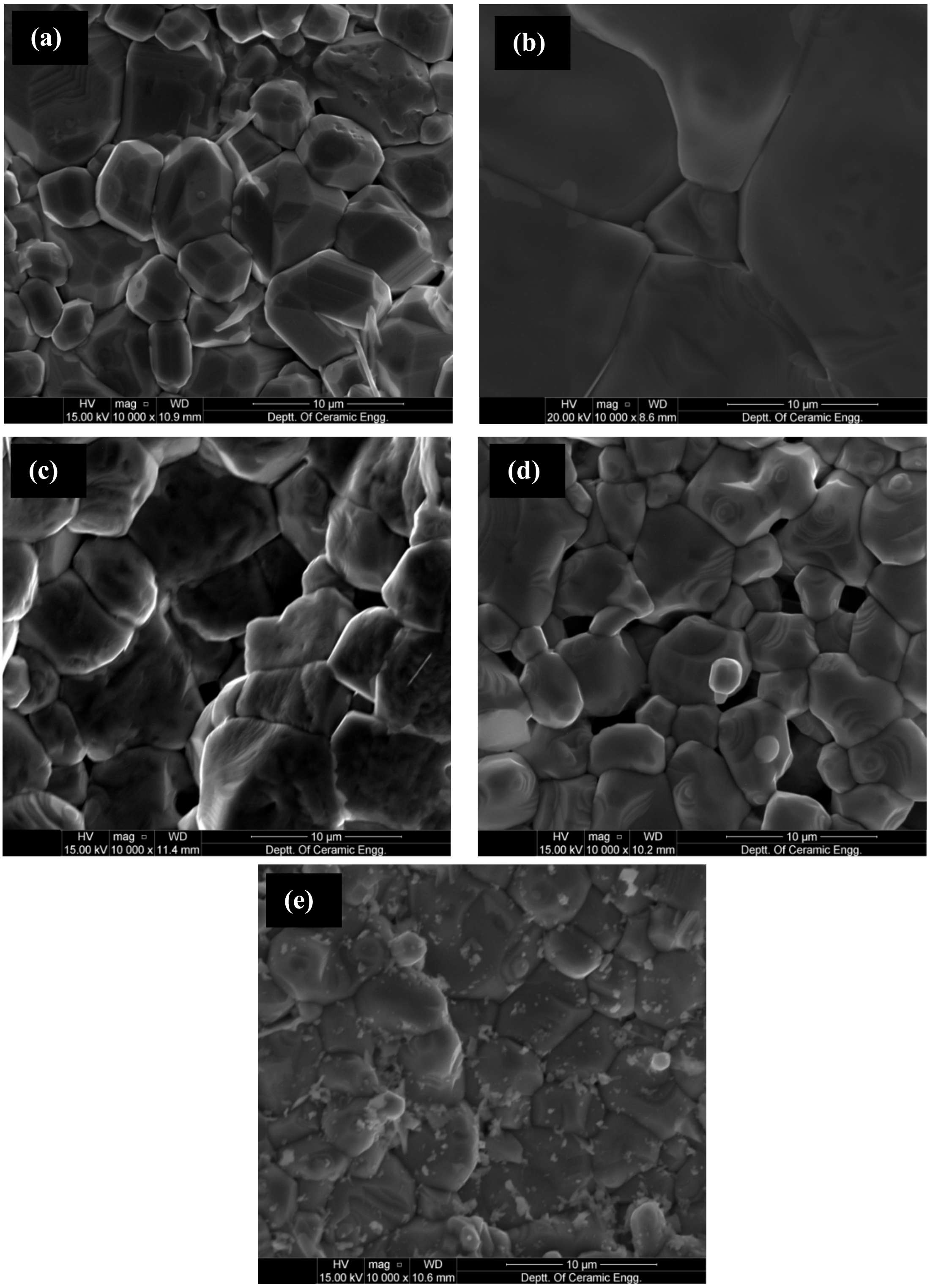

Figure 5.3: SEM micrographs for $Ba_{1-x}Sr_xTiO_3$ (a) x = 0.15, (b) x = 0.20, (c) x = 0.25, (d) x = 0.30 and (e) x=0.35.

5.3.2 Microstructure

The Scanning Electron Micrographs were taken at various magnifications out of which at 10,000 X are presented for the samples in Figures 5.3(a-e). The SEM micrographs show the presence of uniform and well faceted polyhedral grains with minimal voids. The grains have been formed by aggregation of fine particles resulting in regular shape morphology throughout all the compositions. For samples with x=0.15, 0.25, 0.30 and 0.35, the average grain size lies in the range 1 μm to 5 μm which is in agreement with the literature [Zhou et al. (1999); Sonia (2011)]. Density and porosity are given in Table 5.1.

5.3.3 Dielectric characterization (RF Range)

Typical plots for ε' (real part of permittivity) vs. temperature, ε' vs. frequency, loss tangent vs. temperature and loss tangent vs. frequency for all the samples are shown in Figures 5.4, 5.5, 5.6, 5.7 and 5.8. Values of maximum permittivity (ε'_{max}), the corresponding temperature T_m, room temperature values of permittivity (ε'_{RT}) and loss tangent at 1 MHz for all the samples are given in Table 5.2. It is noted that values of T_m decrease almost linearly with increasing x from 373 K for BST15 to 300 K for BST35 as reported in literature [Hilton et al. (1996); Ioachim et al. (2006); Liou et al. (2008)]. T_m decreases at the rate of 3.8 ^{0}C/ mole as shown in Figure 5.9 which agrees well with the reported value [Moulson et al. (2003); Jaffe et al. (1971); Tiwari et al. (1995); Zhou et al. (1999)].

In all the samples the loss tangent is maintained below 0.1 up to 448K and is as low as 0.03 around room temperature for all the frequencies below 1 MHz which indicates that the as prepared material may be used in technological applications.

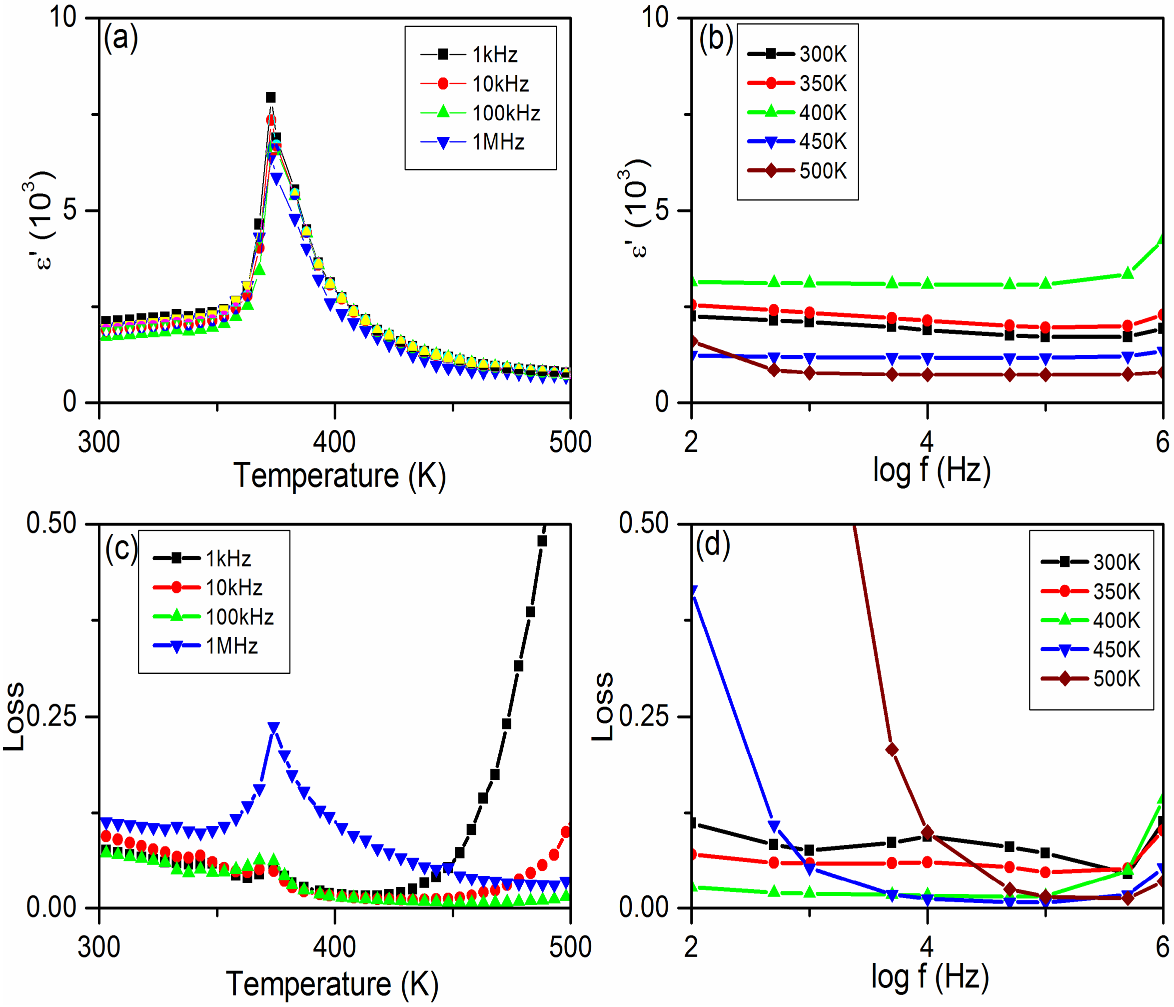

Figure 5.4 : $Ba_{1-x}Sr_xTiO_3$ (x = 0.15) plots for (a) Permittivity (ε′) vs. Temperature at various frequencies (b) Permittivity (ε′) vs. log f at various temperature (c) Dielectric loss vs. Temperature at various frequencies (d) Dielectric loss vs. log f at various temperatures.

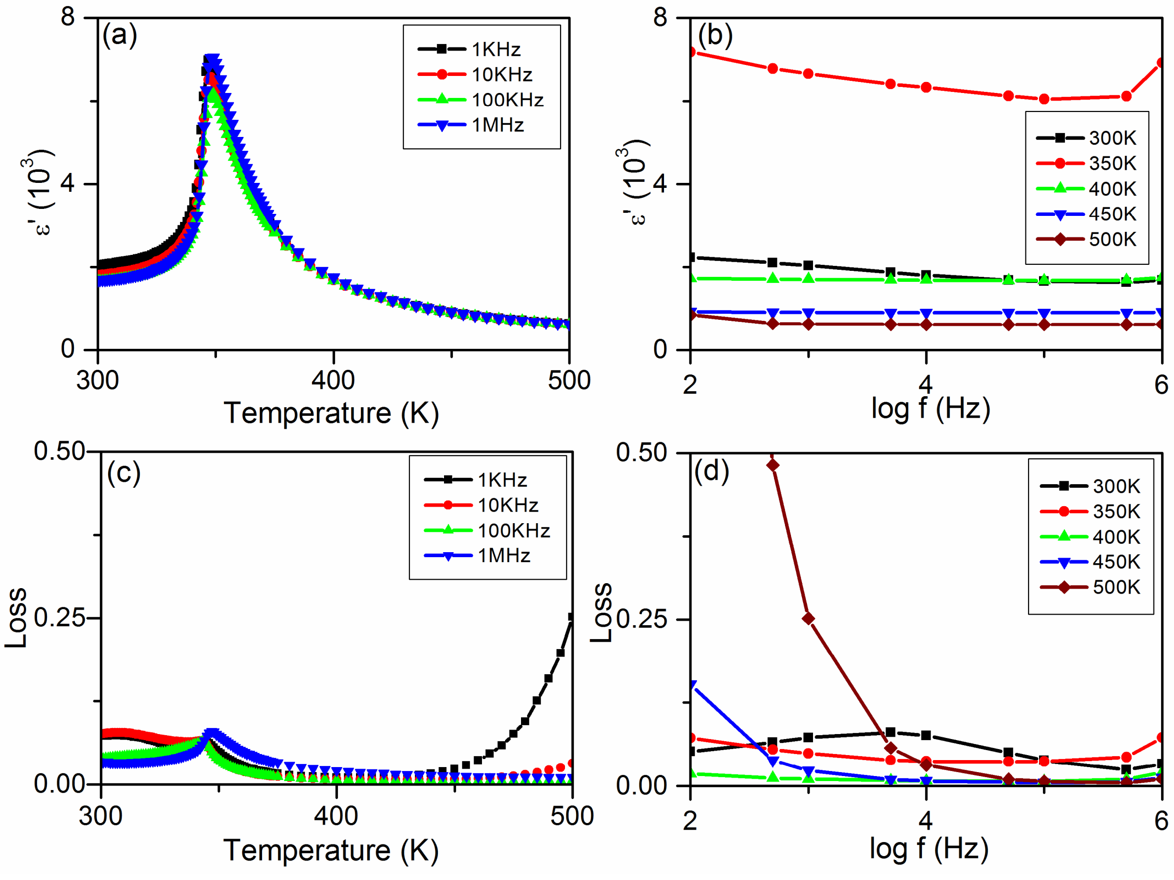

Figure 5.5: $Ba_{1-x}Sr_xTiO_3$ (x = 0.20) plots for (a) Permittivity (ε′) vs. Temperature at various frequencies (b) Permittivity (ε′) vs. log f at various temperature (c) Dielectric loss vs. Temperature at various frequencies (d) Dielectric loss vs. log f at various temperatures.

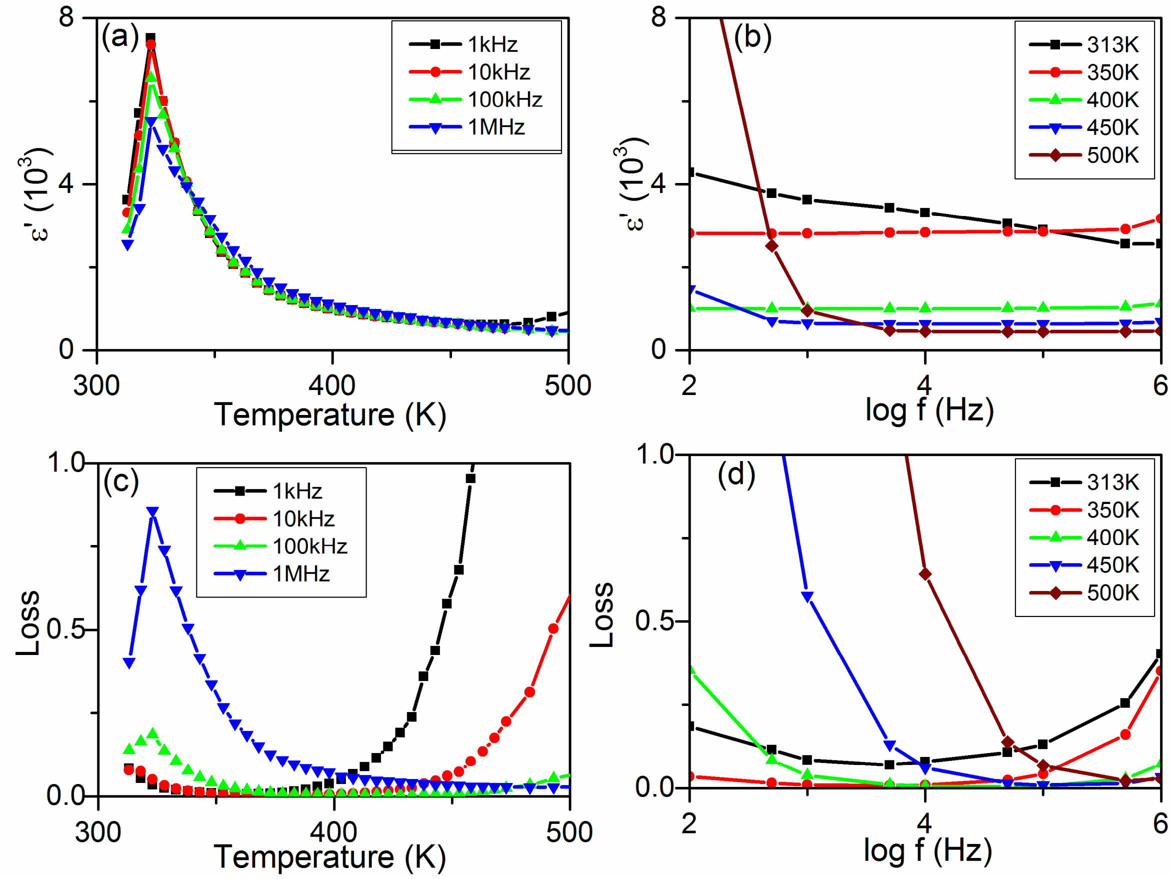

Figure 5.6: $Ba_{1-x}Sr_xTiO_3$ ($x = 0.25$) plots for (a) Permittivity (ε′) vs. Temperature at Various frequencies (b) Permittivity (ε′) vs log f at various temperature (c) Dielectric loss vs. Temperature at various frequencies (d) Dielectric loss vs. log f at various temperatures.

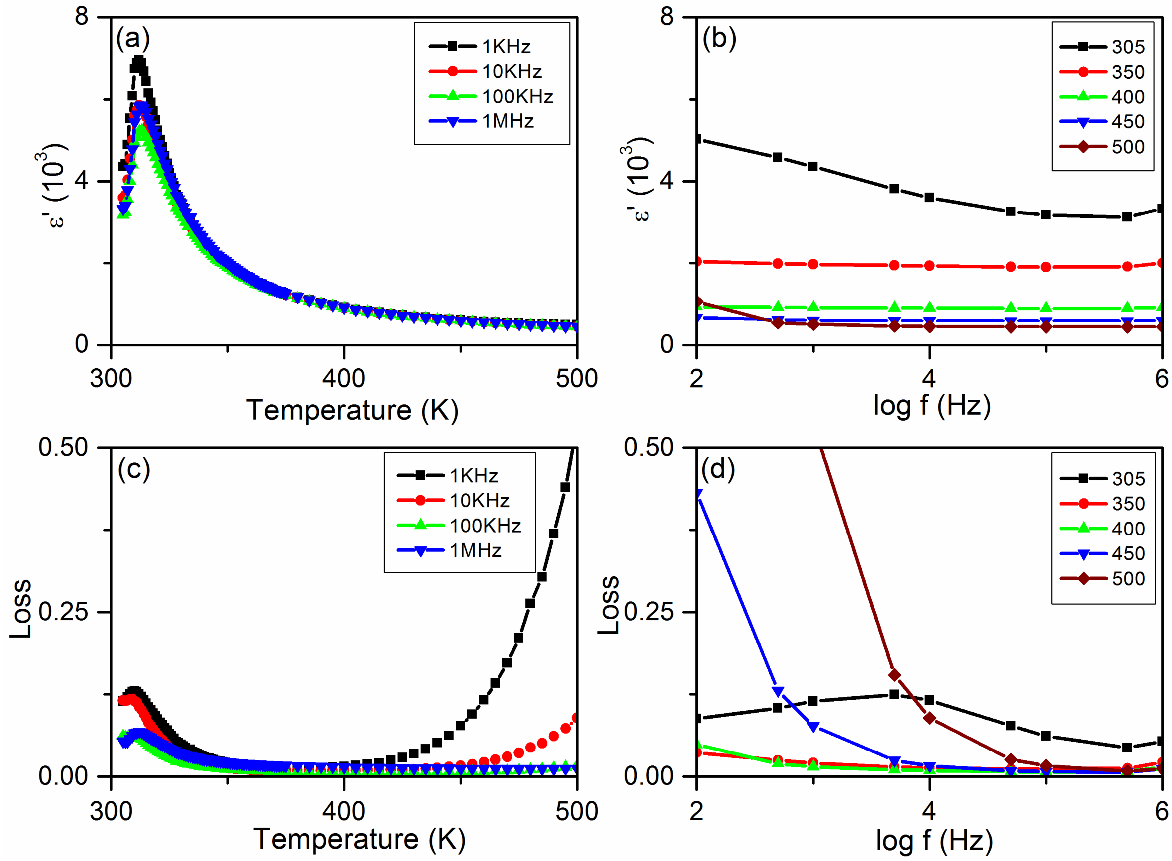

Figure 5.7: $Ba_{1-x}Sr_xTiO_3$ (x = 0.30) plots for (a) Permittivity (ε′) vs. Temperature at various frequencies (b) Permittivity (ε′) vs. log f at various temperature (c) Dielectric loss
vs. Temperature at various frequencies (d) Dielectric loss vs. log f at various temperatures.

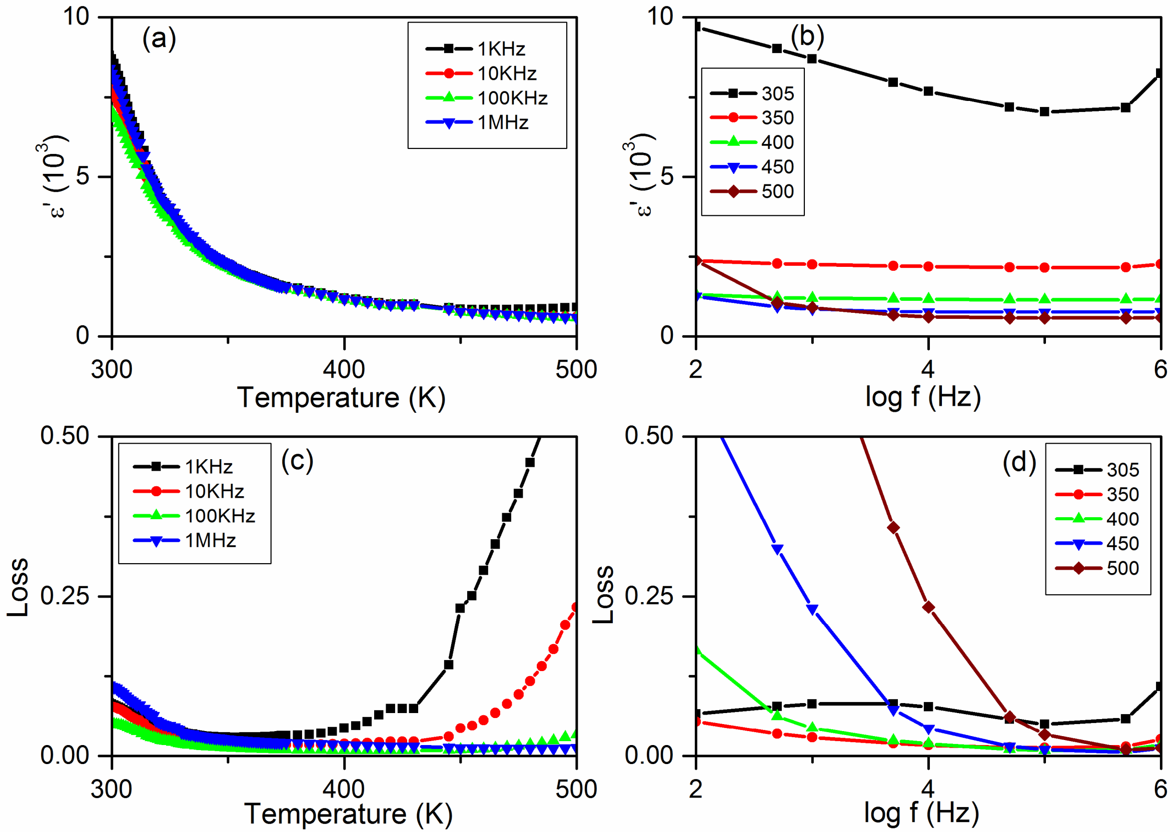

Figure 5.8: $Ba_{1-x}Sr_xTiO_3$ (x = 0.35) plots for (a) Permittivity (ε′) vs. Temperature at various frequencies (b) Permittivity (ε′) vs. log f at various temperatures (c) Dielectric loss vs. Temperature at various frequencies (d) Dielectric loss vs. log f at various temperatures.

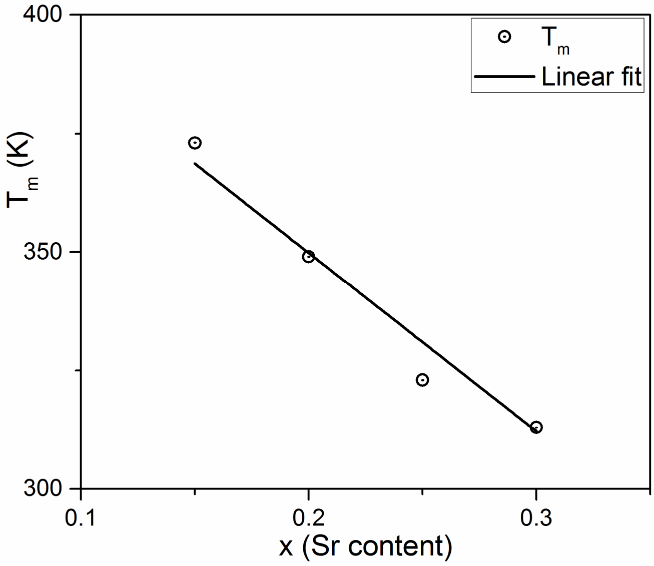

Figure 5.9: Variation of T_m with Sr content

Table 5.2: Dielectric Constant, Loss (at 1MHz, Room Temperature) and Temperature T_m corresponding to ε'_m

Composition(x)	**ε'_m**	**ε'_{RT}**	**loss**	**T_m(K)**
0.15	6390	1930	0.1	373
0.20	7040	1690	0.03	349
0.25	5510	1560	0.4	323
0.30	5850	3320	0.05	313
0.35	8460	8260	0.1	-

It is known that doping of Sr in $BaTiO_3$ leads to broadening of ferroelectric phase transition peak [Jaffe et al. (1971); Tiwari et al. (1995); Dulian (2014); Barb et al. (1982)]. In order to understand the nature of this broadening in our samples $1/\varepsilon'$ vs T was fitted in accordance with the Curie-Weiss law (Equation (5.1))

$$1/\varepsilon' = C/(T-T_C) \quad \ldots(5.1)$$

where C is Curie constant(K^{-1}) and T_C is the Curie Temperature (K).

In all the samples, the data deviated from the Curie-Weiss law as shown in the Figures 5.10 (a-d). This is in agreement with the results reported by other researchers [Tiwari et al. (1995) and references therein] and indicates the presence of diffuse phase transition (DPT). By using the high temperature linear portion of the graphs and a linear fit, the temperature at which the deviation starts (the so-called Burn's temperature, T_B) [Maso et al. (2006)] was obtained as indicated by dotted line in the aforementioned figures.

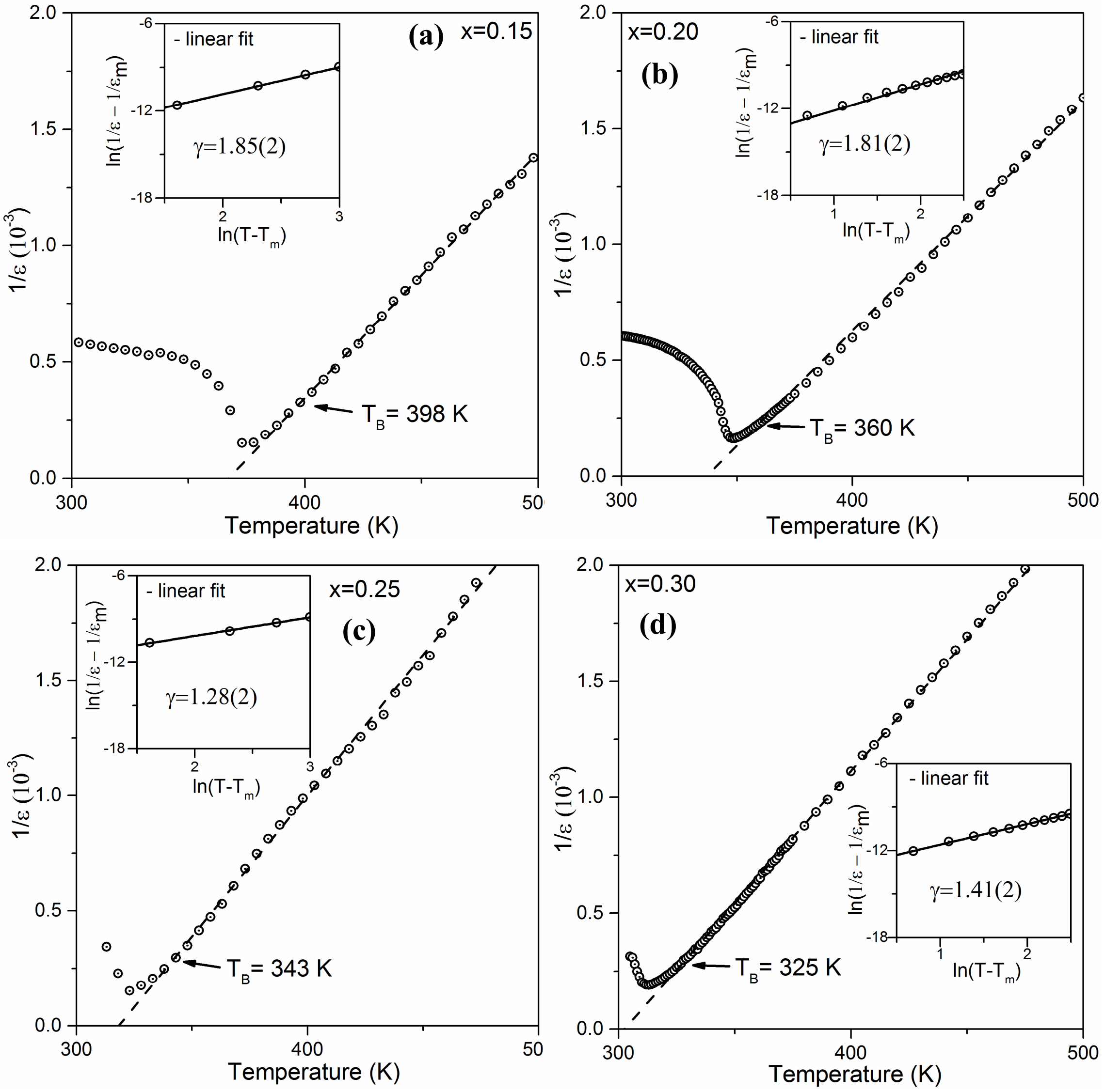

Figure 5.10: Inverse permittivity vs. temperature curve fitted according to Curie-Weiss law
and $\ln(1/\varepsilon' - 1/\varepsilon'_m)$ vs. $\ln(T-T_m)$ curve fitted according to Modified Curie-Weiss law shown in inset for $Ba_{1-x}Sr_xTiO_3$ (a) x = 0.15, (b) x=0.20, (c) x=0.25 and (d) x=0.30.

The degree of diffuseness was estimated by fitting the experimental data to the modified Curie-Weiss law [Uchino et al. (1982)] (Equation (5.2))

$$1/\varepsilon' - 1/\varepsilon'_m = (T-T_m)^\gamma / C, \qquad (T > T_m) \qquad ...(5.2)$$

where ε'_m is the maximum permittivity , T_m is the corresponding temperature and γ is a measure of degree of diffusivity parameter. Here $\gamma = 1$ corresponds to normal ferroelectric phase transition, $\gamma = 2$ to the so called complete relaxor behaviour while $1< \gamma < 2$ indicates Diffuse Phase Transition (DPT). The values of γ were obtained by fitting the experimental values of $\ln(1/\varepsilon' - 1/\varepsilon'_m)$ vs. $\ln(T-T_m)$ in accordance with Equation (5.2) in the temperature range T_m to T_B (Inset of Figures 5.4-5.8).

The best fit values for ε'_m, T_m, γ and C were obtained at 100 kHz and are given in Table 5.3. The value of γ calculated above indicates that samples exhibit DPT behavior. It may be mentioned that displacive ferroelectrics such as barium titanate exhibit Curie constant of the order of 10^5 [Jaffe et al. (1971)]. Higher values of Curie constant are a signature of DPT [Uchino et al. (1982)].

Table 5.3: The best fit values for ε'_m, T_m , γ and C at 100 kHz for $Ba_{1-x}Sr_xTiO_3$ (x= 0.15,
0.20, 0.25 and 0.30) in accordance with modified Curie-Weiss Law (Equation (5.2))

Composition(x)	**ε'_m**	**T_m (K)**	**T_B (K)**	**$\Delta T = T_B - T_m$**	**γ**	**C (10^6 K^{-1})**
0.15	6625	373	398	25	1.85	2.10
0.20	6183	348	360	12	1.81	1.13
0.25	6549	323	343	20	1.28	0.33
0.30	5228	313	325	12	1.41	0.44

5.3.4 Impedance Spectroscopy and Equivalent Circuit Modeling

Complex impedance data taken as a function of frequency and temperature were analyzed for all the samples and equivalent circuit models representing the behavior were obtained. As most of the applications employ the barium strontium titanate system in the paraelectric state, attention was paid towards the high temperature data and equivalent circuit models were developed. Typical plots of Z'' vs. Z' , Z' vs. log f and Z'' vs log f for all the samples at 623 K are shown in Figures 5.11(a,b) – 5.15(a,b).

An electroded ceramic sample in general can be visualized as grain – grain boundary – electrode system having three charge transfer processes with different time constants [Moulson et al. (2003); Macdonald et al. (2005)].

As the plot shown in Figure 5.12(a) does not contain any low frequency rising branch or shift in the high frequency side, presence of series resistance or series capacitance in the equivalent circuit model is ruled out [Pandey et al. (2017); Macdonald et al. (2005); Pandey et al. (1995)]. Also, the plot does not contain any linear branch indicating that the model being sought for would not contain a series CPE (constant phase angle element). Following the steps prescribed by Pandey et al (2017), a model having three parallel RC's , corresponding to grain, grain boundary and electrode processes , connected in series [Moulson et al. (2003)] may be considered. However, as the system at hand shows a diffuse phase transition, there might remain some polar regions here and there still above the transition temperature. This would lead to some distribution in time constants. Therefore, a generalized model in which the C's are replaced by Constant Phase angle Element (CPE) [Macdonald et al. (2005)] is chosen as schematically shown in Figure 5.12. Thus the model used in the analysis involves three parallel R-CPE's connected in series i.e. (R_1-CPE_1)-(R_2-CPE_2)-(R_3-

CPE_3) where it is assumed that R_1-CPE_1 and R_2-CPE_2 correspond to grain and grain boundary respectively and R_3-CPE_3 to the sample- electrode interface.

The impedance Z^* (= Z' - j Z'') of a series combination of parallel R_1 – CPE_1, parallel R_2 – CPE_2 and parallel R_3 – CPE_3 is given below [Pandey et al. (2017); Macdonald et al. (2005)]

$$Z^* = \frac{R_1}{1+A_{01}R_1(j\,\omega)^{\Psi_1}} + \frac{R_2}{1+A_{02}R_2(j\,\omega)^{\Psi_1}} + \frac{R_3}{1+A_{03}R_3(j\,\omega)^{\Psi_3}} \quad \ldots (5.3)$$

$$= \frac{R_1}{1+(j\,\omega\,\tau_1)^{\Psi_1}} + \frac{R_2}{1+(j\,\omega\,\tau_2)^{\Psi_1}} + \frac{R_3}{1+(j\,\omega\,\tau_3)^{\Psi_3}} \quad \ldots (5.4)$$

where $\tau_1 = (A_{01} R_1)^{(1/\Psi1)}$, $\Psi_1 = 1-\theta_1/(\pi/2)$ … (5.5)

. $\tau_2 = (A_{02} R_2)^{(1/\Psi2)}$, $\Psi_2 = 1-\theta_2/(\pi/2)$ … (5.6)

. $\tau_3 = (A_{03} R_3)^{(1/\Psi3)}$, $\Psi_3 = 1-\theta_3/(\pi/2)$ … (5.7)

A_{01},A_{02} and A_{03} are parameters which have dimension of capacitance when ψ's is equal to 1. θ_1 , θ_2 and θ_3 are angles as described below. R_1, R_2 and R_3 are in ohms and τ_1, τ_2 and τ_3 are time constants in seconds.

It is known that two distinct depressed semicircular arcs appear in Z'' vs. Z' plot for an equivalent circuit model containing parallel R_1-CPE_1 and parallel R_2-CPE_2 circuits connected in series, when their response frequencies are widely separated. If we assume that response frequencies of R_1-CPE_1 are much higher than those of R_2-CPE_2 , then θ_1 would be the angle between Z' axis and the line joining the centre, ($R_1/2$, -($R_1/2$) tan θ_1), of the depressed circular arc corresponding to R_1-CPE_1 , to the origin in the Z'' vs Z' plot. This arc would pass through origin at the high frequency side and will intercept the Z'axis at the point (R_1,0) at the low frequency side. Then , θ_2 would be the angle between Z' axis and the line joining the centre ($R_2/2$, $-(R_2/2) \tan \theta_2$) , of the depressed low frequency side circular arc corresponding to R_2-CPE_2, to the point (R_1,0) . The overall low frequency intercept of this combination will be at the point ($R_1 + R_2$,0). Similarly, if $R_3 - CPE_3$ having the largest time constant is also present in series in the equivalent circuit , θ_3 would be the angle between Z' axis and the line joining the centre , ($R_3/2$, $-(R_3/2) \tan \theta_3$) , of the depressed lowest frequency side circular arc corresponding to R_3-CPE_3, to the point ($R_1 + R_2$,0). The overall low frequency intercept of this combination will then be at the point ($R_1 + R_2 + R_3$, 0) and the Z'' vs Z' plot would contain three distinct clearly visible depressed arcs when the response times are widely separated [Pandey et al. (2017); Macdonald et al. (2005)].

The initial values of the parameters of Equation (5.3) were estimated by drawing three joined tentative arcs (as shown in Figure 5.12(a)) and by finding the intercepts on the Z' axis , the coordinates of the centres of tentative depressed arcs and the frequencies where the Z'' peaks [Pandey et al. (2017)]. Using these as initial guesses, the values of the components were determined more accurately by using the EIS Spectrum Analyzer 1.0 software [Bondarenko et al. (2005)]. The fitted values are also shown in Figure 5.11(a,b). Data for all the samples were analyzed in this way and are given in Figures 5.11-5.15. Typical values of the components for all the samples are given in Tables 5.4 – 5.8.

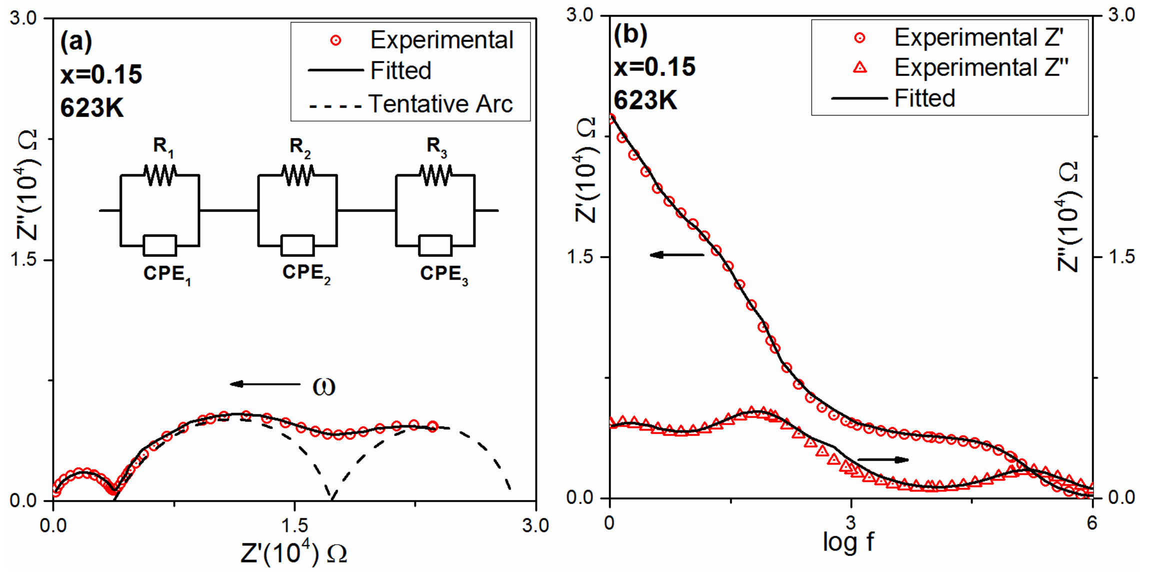

Figure 5.11: Experimental and fitted plots of (a) Z″ vs. Z′ (b) Z′, Z″ vs. log f at 623 K for $Ba_{1-x}Sr_xTiO_3$ (x = 0.15)

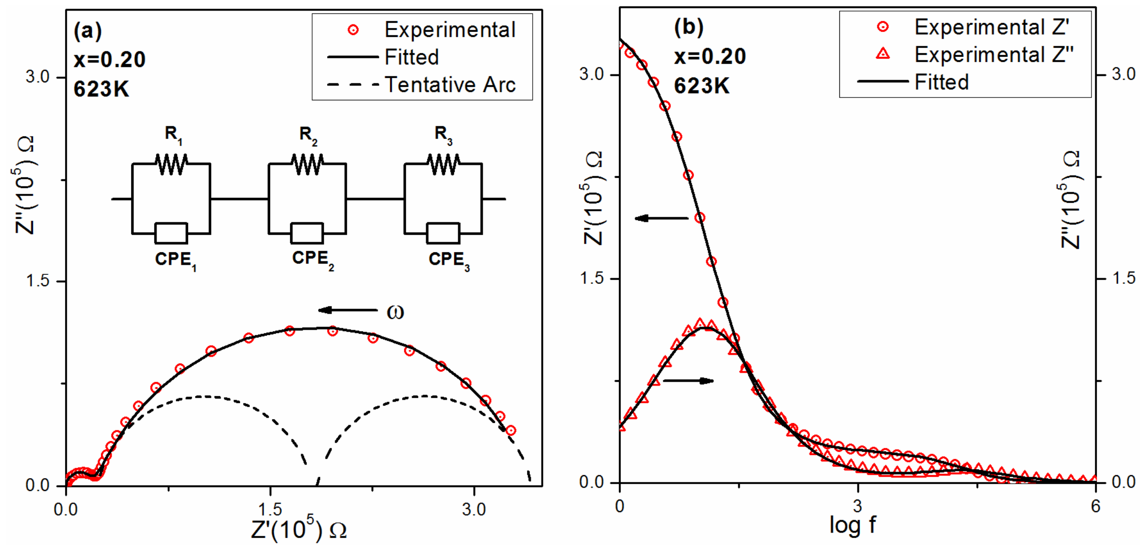

Figure 5.12: Experimental and fitted plots of (a) Z″ vs. Z′ (b) Z′, Z″ vs. log f at 623 K for $Ba_{1-x}Sr_xTiO_3$ (x = 0.20)

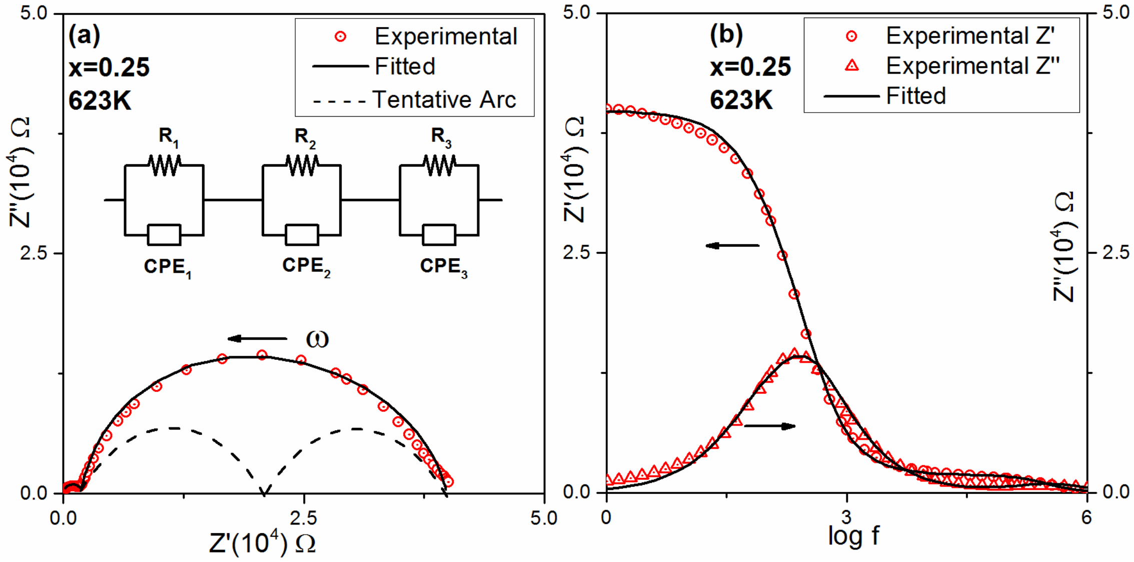

Figure 5.13: Experimental and fitted plots of (a) Z″ vs. Z′ (b) Z′, Z″ vs. log f at 623 K for $Ba_{1-x}Sr_xTiO_3$ (x = 0.25)

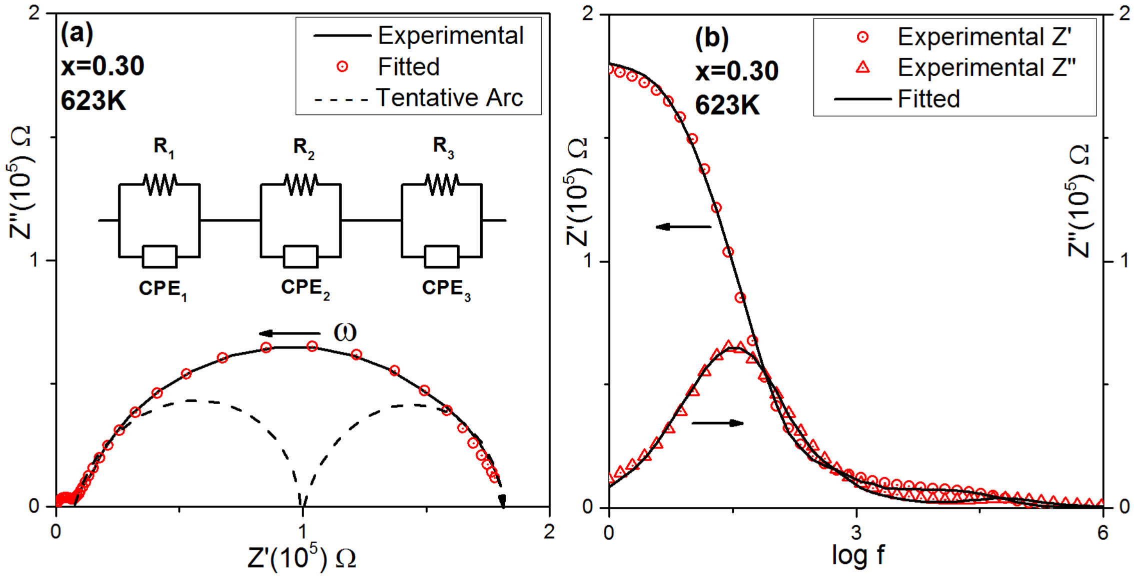

Figure 5.14: Experimental and fitted plots of (a) Z″ vs. Z′ (b) Z′, Z″ vs. log f at 623 K for $Ba_{1-x}Sr_xTiO_3$ (x = 0.30)

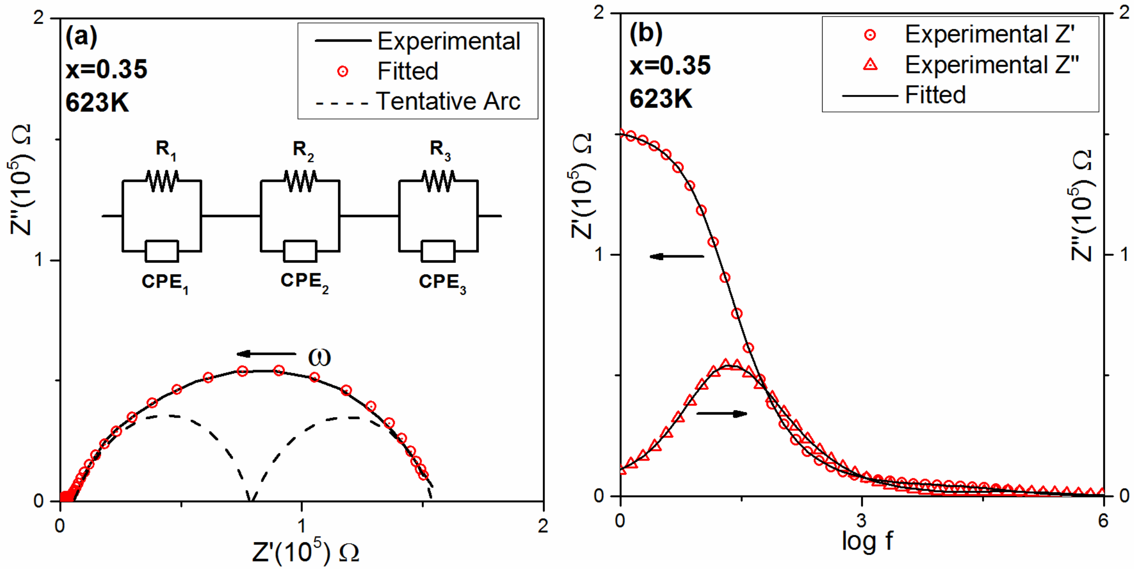

Figure 5.15: Experimental and fitted plots of (a) Z″ vs. Z′ (b) Z′, Z″ vs. log f at 623 K for $Ba_{1-x}Sr_xTiO_3$ (x = 0.35)

The values of χ^2 (indicating the goodness of fit) for all the samples are below 0.05.

Table 5.4: Values of the components of the model for BST15

T (K)	**R_1 (kΩ)**	**ψ_1**	**A_{01} (10^{-10})**	**R_2 (kΩ)**	**Ψ_2**	**A_{02} (10^{-7})**	**R_3 (kΩ)**	**Ψ_3**	**A_{03} (10^{-7})**
573	20.71 ±1.38	0.96 ±0.06	3.98 ±0.62	49.02 ±1.8	0.87 ±0.01	3.05 ±0.23	49.83 ±5.0	0.75 ±0.03	19.60 ±4.1
623	3.74 ±0.21	0.95 ±0.07	5.38 ±0.89	13.70 ±0.36	0.79 ±0.02	3.54 ±0.40	11.32 ±2.76	0.79 ±0.04	100.00 ±15.97
673	0.87 ±0.01	0.95 ±0.01	5.46 ±1.02	3.76 ±0.09	0.77 ±0.01	8.22 ±0.01	4.16 ±0.16	0.75 ±0.01	277.27 ±6.54
723	0.28 ±0.01	0.91 ±0.12	6.08 ±0.34	1.20 ±0.02	0.77 ±0.01	7.63 ±0.85	1.34 ±0.09	0.73 ±0.02	372.47 ±32.36

Table 5.5: Values of the components of the model for BST20.

T (K)	**R_1 (kΩ)**	**ψ_1**	**A_{01} (10^{-10})**	**R_2 (kΩ)**	**Ψ_2**	**A_{02} (10^{-7})**	**R_3 (kΩ)**	**Ψ_3**	**A_{03} (10^{-7})**
573	107.00	0.82	24.21	791.00	0.84	1.00	890.00	0.80	1.92
	±2.76	±0.01	±2.35	±10.84	±0.01	±0.02	±19.66	±0.01	±0.03
623	22.16	0.86	17.51	200.03	0.84	1.00	124.57	0.80	4.65
	±1.14	±0.02	±5.32	±1.83	±0.01	±0.03	±2.37	±0.01	±0.19
673	4.17	0.97	17.50	43.09	0.82	1.10	28.42	0.77	8.01
	±0.72	±0.001	±0.03	±1.14	±0.09	±0.05	±3.52	±0.02	±0.76
723	1.09	0.83	36.02	13.55	0.81	1.30	5.27	0.80	9.13
	±0.09	±0.03	±0.22	±0.15	±0.01	±0.07	±0.25	±0.02	±0.08

Table 5.6 : Values of the components of the model for BST25.

T (K)	**R_1 (kΩ)**	**ψ_1**	**A_{01} (10^{-10})**	**R_2 (kΩ)**	**Ψ_2**	**A_{02} (10^{-7})**	**R_3 (kΩ)**	**Ψ_3**	**A_{03} (10^{-7})**
573	107.62	0.83	2.42	791.74	0.85	1.00	890.00	0.80	1.93
	±0.48	±0.01	±0.63	±0.55	±0.01	±0.01	±0.72	±0.01	±0.05
623	1.82	0.99	2.97	23.26	0.91	0.38	14.77	0.84	3.03
	±0.17	±0.07	±0.62	±0.21	±0.01	±0.04	±0.32	±0.03	±0.84
673	1.04	0.99	97.90	5.50	0.99	1.10	3.21	0.64	19.53
	±0.03	±0.02	±0.07	±0.01	±0.03	±0.02	±0.04	±0.06	±0.19
723	0.51	0.99	246.19	2.67	0.85	0.96	0.32	0.99	87.65
	±0.04	±0.28	±16.84	±0.07	±0.01	±0.05	±0.02	±0.03	±3.84

Table 5.7 : Values of the components of the model for BST30.

T (K)	R1 (kΩ)	ψ_1	A_{01} (10^{-10})	R2 (kΩ)	Ψ_2	A_{02} (10^{-7})	R3 (kΩ)	Ψ_3	A_{03} (10^{-7})
573	39.50 ±1.58	1.00 0±.07	4.63 ±0.57	586.45 ±10.93	0.93 ±0.01	0.36 ±0.02	375.33 ±26.05	0.99 ±0.04	1.69 ±0.24
623	7.20 ±0.26	0.99 ±0.08	3.90 ±0.08	104.00 ±1.92	0.92 ±0.01	0.40 ±0.04	71.00 ±2.44	0.90 ±0.02	2.72 ±0.32
673	1.50 ±0.06	0.99 ±0.04	3.47 ±0.31	21.13 ±0.30	0.80 ±0.01	1.36 ±0.06	11.50 ±0.33	0.80 ±0.01	4.47 ±0.40
723	0.58 ±0.08	1.00 ±0.03	3.03 ±0.02	7.80 ±0.11	0.79 ±0.01	1.50 ±0.07	3.04 ±0.13	0.80 ±0.01	9.56 ±0.12

Table 5.8 : Values of the components of the model for BST35.

T (K)	R1 (kΩ)	ψ_1	A_{01} (E-10)	R2 (kΩ)	Ψ_2	A_{02} (E-8)	R3 (kΩ)	Ψ_3	A_{03} (E-7)
573	20.03 ±1.29	0.89 ±0.03	6.33 ±0.12.	507.40 ±44.56	0.85 ±0.02	4.78 ±0.34	168.89 ±13.55	0.57 ±0.07	7.57 ±0.30
623	5.30 ±0.34	0.88 ±0.02	5.87 ±0.09	105.15 ±8.62	0.89 ±0.02	3.97 ±0.55	47.19 ±1.89	0.61 ±0.05	8.15 ±0.28
673	1.50 ±0.23	0.99 ±0.20	4.05 ±0.08	24.72 ±0.41	0.86 ±0.05	7.72 ±0.34	12.22 ±0.98	0.95 ±0.01	3.39 ±0.29
723	0.42 ±0.02	0.95 ±0.07	3.69 ±0.20	4.58 ±0.11	0.95 ±0.01	3.10 ±0.25	2.71 ±0.24	0.91 ±0.02	3.91 ±0.24

An attempt was made to explore whether any empirical relation could be established for the values of the components of the model with temperature T and composition x. For this, the resistive components were considered. The values of $\log_e(R_1)$, $\log_e(R_2)$ and $\log_e(R_3)$ were plotted vs 1000/T so that if these plots are straight lines, dependence of $\log_e(R_1)$, $\log_e(R_2)$ and $\log_e(R_3)$ on T is established in the form of Arrhenius equation as given below (Equation (5.8) where k is Boltzmann constant and R_0 is pre-exponential factor. Equation (5.8) can be written as -

$$\log_e(R) = \text{slope} * (1000/T) + \text{intercept}$$

…(5.9)

where slope = $(E_a/1000k)$ and intercept = $\log_e R_0$ for $\log_e(R)$ vs (1000/T) plot, E_a being the activation energy.

Typical plots of $\log_e(R)$ vs 1000/T with $R = R_1$, R_2 and R_3 corresponding to $x = 0.30$ are shown in Figure 5.16 which are straight lines that may be expressed mathematically by Equation (5.9). The plots for other values of x were similar to this and are not shown. The values of slope and intercept were noted down. Now let us consider the case of R_1. The values of slope and intercept obtained above for R_1 were plotted as a function of x and were found to be linear as shown in Figure 5.17. From this, the relations between slope and x and between intercept and x were established. These plots for R_2 and R_3 were similar to this and are not shown. Thus the values of R_1, R_2 and R_3 appearing in Equation (5.3) for the impedance of the equivalent circuit model as shown in Figure 5.11 were obtained in terms of temperature and composition and are given below in Equations (5.10-5.12):

$$R_1(x) = \exp[(20.0x - 18.1)] \exp[(-12.9x + 16.4)(1000/T)] \quad \ldots(5.10)$$

$$R_2(x) = \exp[(-0.8x - 7.7)] \exp[(4.7x + 12.5)(1000/T)] \quad \ldots(5.11)$$

$$R_3(x) = \exp[(0.7x - 7.5)] \exp[(1.7x + 10.9)(1000/T)] \quad \ldots(5.12)$$

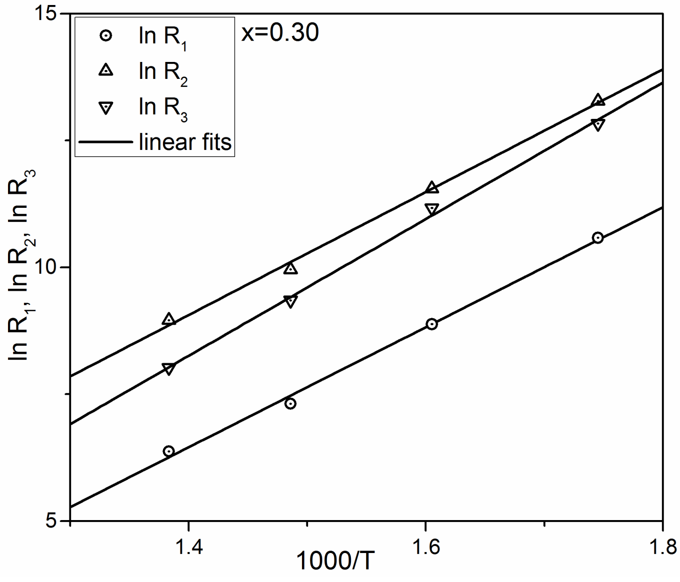

Figure 5.16: Plots of ln(R_1), ln(R_2) and ln(R_3) vs. 1000/T for BST30.

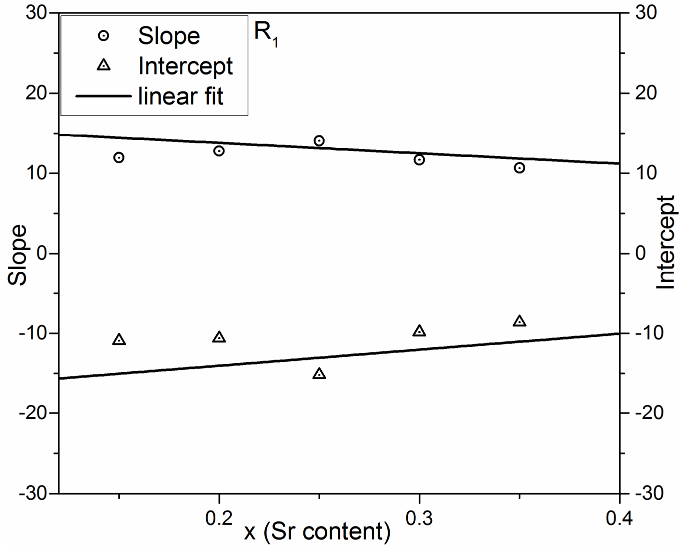

Figure 5.17: Variation of slope and intercept (obtained in Figure 5.16) with x (Sr content) for R_1.

Activation energies corresponding to R_1, R_2 and R_3 are (-12.9 x + 16.4) * 0.086 eV, (4.7 x + 12.5) * 0.086 eV and (1.7 x + 10.9) * 0.086 eV i.e. (-1.1 x + 1.4) eV, (0.4 x + 1.0) eV and (0.1 x + 0.9) eV respectively. Thus as x increases, activation energy for R_1 (i.e. grains) decreases where as for R_2 (i.e. grain boundary) and R_3 (i.e. electrode interface) increases. The impedance analysis was carried out for temperatures above the transition temperature as mentioned earlier.

5.3.5 P-E Hysteresis

The P-E hysteresis plots at an applied field up to 12 KV/cm are given in Figure 5.18 .All the samples show normal ferroelectric P vs E hysteresis behaviour. It is easily observable that as the Sr content is increased, the hysteresis loop becomes thinner i.e. the BST material becomes softer. This is because addition of Sr leads to free movement of the domain walls which leads to easy orientation. Most of the PE loops are not fully saturated probably due to leakage current but these are definitely tending towards saturation. The approximate saturation polarization (P_s) , retentivity (P_r) and coercivity (E_c) for all the samples are presented in Table 5.9. These qualitatively match with those reported by Puli et al. (2017) and Singh et al. (1996) and are higher than those reported by Curecheriu et al. (2009) and Liou et al. (1997). It can be seen that addition of Sr leads to reduction of P_s, P_r and E_c, This agrees with findings by Kim et al. (2013).

Table 5.9 :Approximate Saturation Polarization (P_s) , Retentivity (P_r) and Coercivity (E_c) for all the samples

Composition(x)	**Approximate Saturation Polarization (P_s) (μC/cm^2)**	**Retentivity (P_r) (μC/cm^2)**	**Coercivity (E_c) (KV/cm)**
0.15	9.53	5.17	2.89
0.20	9.23	4.19	2.26
0.25	8.42	1.82	1.14
0.30	7.96	1.21	0.56
0.35	6.06	0.58	0.28

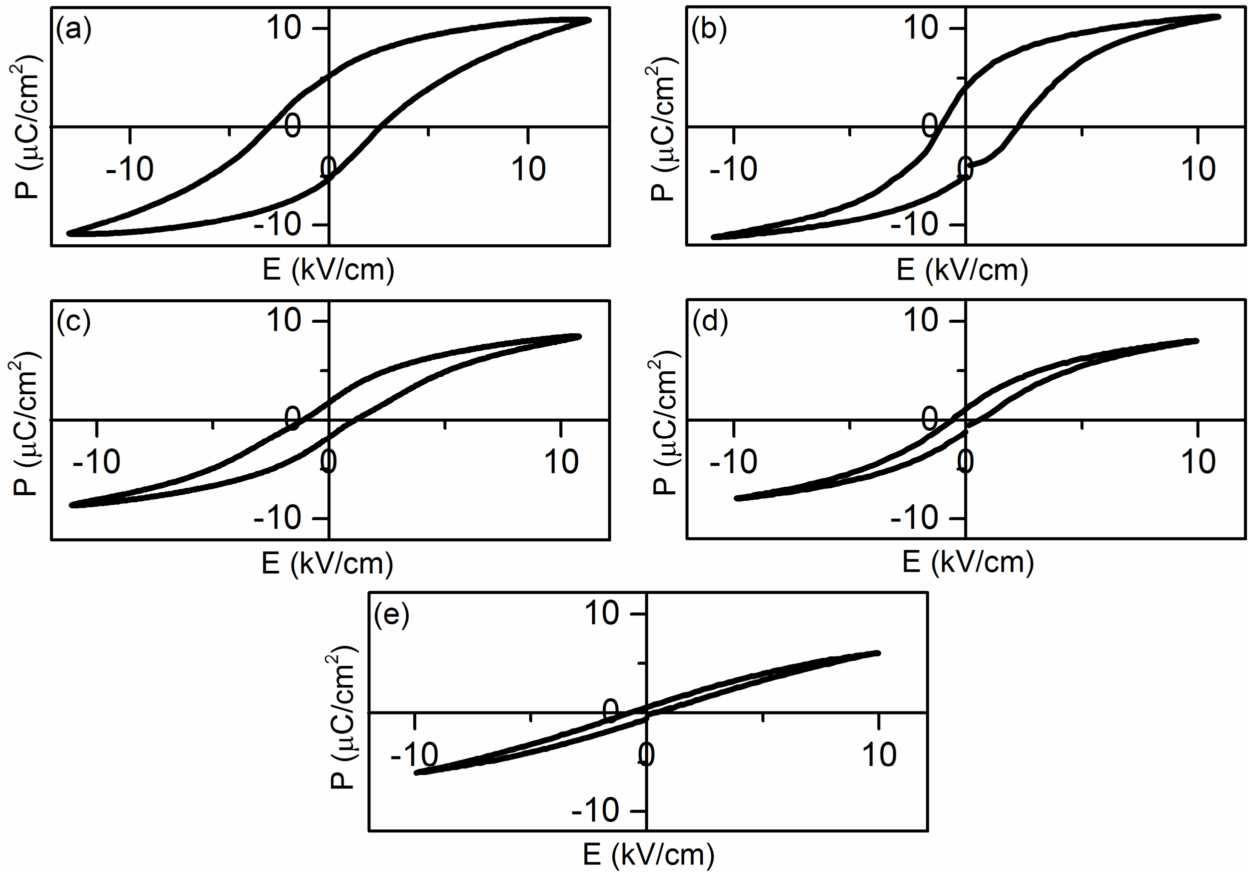

Figure 5.18: P-E Hysteresis loop for $Ba_{1-x}Sr_xTiO_3$ (a) x = 0.15, (b) x = 0.20, (c) x = 0.25, (d) x = 0.30 and (e) x = 0.35.

5.3.6 Dielectric characterization (Microwave Range)

Variations of dielectric constant and dielectric loss in the frequency range 8 – 12 GHz measured at room temperature are shown in Figure 5.19 for x = 0.15 (BST15), 0.20 (BST20), 0.25 (BST25), 0.30 (BST30) and 0.35 (BST35). The values of permittivity obtained here are in the range 32 to 42 and loss in the range 0.15 to 0.35. Ioachim et al. (2006) have reported permittivity in the range 910-1746 and loss in the range 0.18-14 for the compositions $0.25 \leq x \leq 0.75$ at 1GHz. All the samples do not show large variations with frequency and may be used in microwave applications. It is seen that as x increases, ε′ first decreases and then increases.

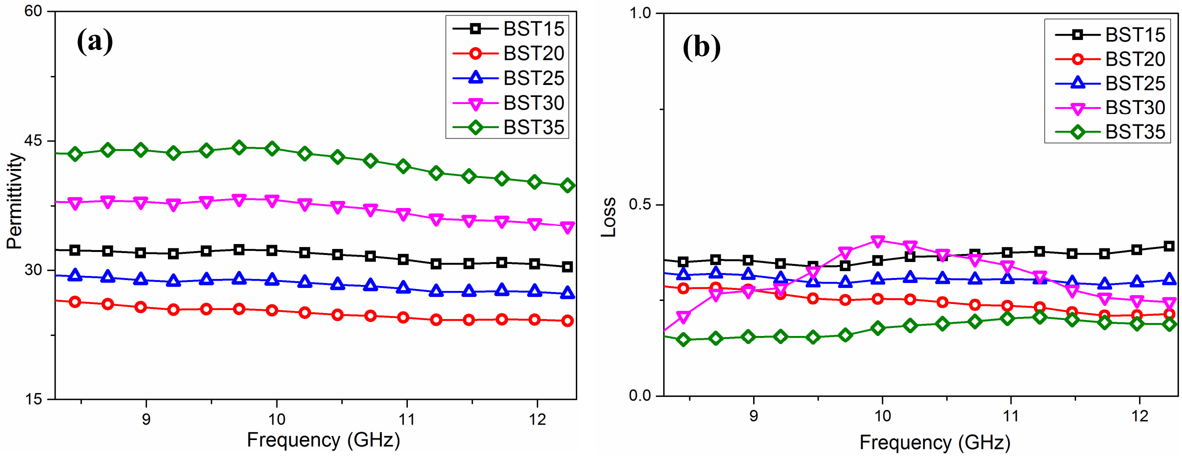

Figure 5.19: (a) Permittivity vs. frequency and (b) loss vs. frequency plots for $Ba_{1-x}Sr_xTiO_3$ for x = 0.15, 0.20, 0.25, 0.30 and 0.35 in X-Band.

5.4 Conclusion

In conclusion compositions with x = 0.15, 0.20, 0.25, 0.30 and 0.35 in the system $Ba_{1-x}Sr_xTiO_3$ were synthesized using conventional solid state reaction method and characterized by XRD and SEM. Rietveld refinement of the XRD patterns confirmed the presence of single tetragonal phase for all the compositions. Dielectric and impedance measurements were carried out in the temperature range 300K – 723 K. As x increases the temperature of permittivity maxima decreases almost linearly. All the samples exhibit diffuse phase transition. An equivalent circuit model comprising three parallel combinations of resistance and constant phase angle element viz (R_1 – CPE_1) – (R_2-CPE_2) – (R_3-CPE_3) , corresponding to grain, grain boundary and electrodes, was developed that represented the data well. Empirical expressions for the values of R_1, R_2 and R_3 were obtained in terms of temperature and composition. This may be useful in design and simulation studies. Activation energies corresponding to R_1, R_2 and R_3 are ($-1.1\,x + 1.4$) eV, ($0.4\,x + 1.0$) eV and ($0.1\,x + 0.9$) eV respectively. Thus as x increases, activation energy for R_1 (i.e. grains) decreases where as for R_2 (i.e.

grain boundary) and R_3 (i.e. electrode interface), it increases. P vs. E loops for all the samples indicate a normal ferroelectric behavior. The values of dielectric permittivity measured in the frequency range 8-12 GHz in the X band of microwaves are around 32, 28, 25, 35 and 42 for x equal to 0.15, 0.20, 0.25, 0.30 and 0.35 respectively and are almost independent of frequency with the loss being in the range 0.4 to 0.1.